Experimental Investigations of an Internal Flow Generated by Porous Injection

Clarisse Fournier

Marc Michard

CETHIL-UMR CNRS 5008,
INSA Lyon,
Bat Sadi Carnot, 20 av. Albert Einstein,
69621 Villeurbanne Cedex, France

Françoise Bataille[1]
PROMES-UPR CNRS 8521,
Rambla de la Thermodynamique,
Tecnosud, 66100 Perpignan, France
e-mail: francoise.daumas-bataille@univ-perp.fr

An anisothermal channel flow generated by a porous injection is investigated in details for different Reynolds numbers of the injection in order to highlight the impact of the microstructure of porous material on the flow development. Two types of porous materials, being characterized by different matrices and pore sizes are studied: a coarse bronze porous plate (30% porosity and 100 μm average pore diameter) and a stainless steel porous plate (30% porosity and 30 μm average pore diameter). Particle image velocimetry, hot-wire anemometry, and cold wire thermometer measurements lead to the comparison of mean profiles, rms profiles, and energy spectra for the velocity and temperature fields. Two-point spatial correlations for the fluctuating velocity are also calculated. In the case of the coarse bronze plate, the flow is slightly fluctuating with big space coherence. In the opposite, the results obtained with the fine pore plate show a flow close to a fully developed turbulent channel flow. The comparison of the aerodynamic field with computational simulations based on a Reynolds-averaged Navier-Stokes (RANS) model underlines the difficulties to reproduce exactly the evolution of the mean and fluctuating velocities in all the explored part of the channel. [DOI: 10.1115/1.3197140]

Keywords: blowing, turbulent channel flow, heat transfer, particle image velocimetry, cold wire thermometer

1 Introduction

The flows induced by blowing through permeable walls have been the subject of many isothermal studies due to their importance in various engineering applications. These include, for example, flow filtration process [1] or diffuse separation of gaseous isotopes [2]. In literature, we can find many geometries for modeling the combustion in solid propellant rocket motors with a porous wall through which fluid is normally injected [3–10]. This type of channel flow presents some characteristics quite different from that observed in a pipe or in a boundary layer flow with impermeable walls. Flows generated by wall injection involve two basic characteristics. The first feature of such a flow is the streamline strong curvature. Figure 1 shows the streamlines of the laminar flow, which develops in a channel with a no-slip condition at the upper wall and a uniform positive injection at the lower wall [11]. The effect of the main control parameter, the Reynolds number Re_{in} based on the channel height e and the injection velocity V_{in} is presented. The second important feature of flows generated by wall injection is the acceleration of the flow with the downstream distance x [6,12,13]. Analytical solutions of the laminar, steady, incompressible, and two-dimensional channel flow generated by wall injections were investigated by several authors [1–3]. These solutions are rather close to numerical and experimental results before a critical turbulence threshold implies a transition process of the mean axial velocity. The transition behavior of the velocity field has been numerically investigated by several authors. Eddy viscosity models [5,14] permitted to obtain good comparison of the mean flow characteristics with the experimental data but generally overpredicted turbulence intensity in the channel. Complex RANS simulations based on second-order models [15,16] are better to reproduce the transition process while large eddy simulation (LES) approach [8,17,18] permits to capture vortex structures.

Some discrepancies observed between the numerical and experimental results are mainly due to the boundary conditions on the porous surface [19] and show that large modifications of the flow structure come from the nonideal boundary conditions. These authors studied two different porous walls (honeycombs with a factor of 1.7 between the pore sizes) and observed larger turbulent shear stresses with a coarser porous surface.

In this paper, we present experiments performed in an anisothermal channel flow generated by injection through a porous wall. The aim of this study is to determine how this type of flow develops in the channel. The effect of the microstructure of the porous plate is investigated. The first porous material used is a bronze plate with spherical powders: 30% porosity, 100 μm average pore diameter, and a roughness in the order of 30 μm. The second one is made of sintered stainless steel: 30% porosity, 30 μm average pore diameter, and a roughness in the order of 10 μm. The choice of these two types of materials will be justified a posteriori by the differences observed on the generated flow. The experimental setup permits to investigate the behavior of velocity basic statistics at different sections inside the channel and temperature statistics near the exit. In order to get details about the structure of the flow, we also measured two-point spatial correlations for both porous plates at different injection Reynolds numbers. Finally, we compare results with computations based on RANS simulations.

2 Experimental Facilities

2.1 Test Channel. The main components of the experimental apparatus are schematically shown in Fig. 2. A more complete description of the experimental setup is available in Ref. [20]. Air is injected at 20 °C into the channel through the lower horizontal wall at $y=0$ made of a $495\times200\times3$ mm^3 porous plate. A 150 mm box fitted under the porous plate is designed to deliver a nearly uniform injection flow rate through the porous plate. The

[1]Corresponding author.

Contributed by the Applied Mechanics Division of ASME for publication in the JOURNAL OF APPLIED MECHANICS. Manuscript received March 27, 2008; final manuscript received July 1, 2009; published online December 21, 2009. Review conducted by Nesreen Ghaddar.

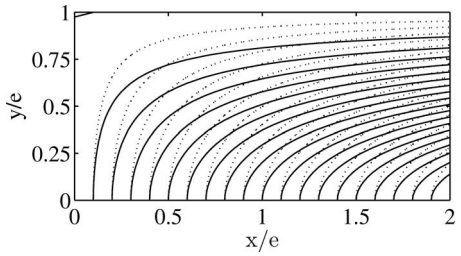

Fig. 1 Streamlines – –:Re_{in}=1 and —:Re_{in}=1000

upper wall of the channel consists of an impermeable thin stainless steel foil (50 μm thickness) heated by Joule effect. A heat insulator is placed over the heated wall in order to prevent heat loss by conduction. The channel height e is equal to 10 mm giving a length to height ratio of 50. The channel is closed at $x=0$ by an impermeable vertical wall thermally insulated with Teflon. The channel is limited in the spanwise direction z by glass windows in order to permit optical measurements using particle image velocimetry (PIV). The main control parameter of the dynamic flow is a Reynolds number Re_{in} based on the vertical injection velocity V_{in} and the height e of the channel; experiments conducted for $63 < Re_{in} < 220$ are presented in this paper. In this range of Reynolds numbers, the temperature boundary layer near the upper wall is thin and the temperature of the injected fluid is supposed to be nearly equal to the temperature of the porous plate. In the present experiment, the temperature difference between the upper wall and the injected air is 45°C.

2.2 Techniques Measurements and Postprocessing. Instantaneous velocity fields are measured by particle image velocimetry in the $(x-y)$ plane (comparison was shown in Fig. 3), in the symmetry plane $z=0$ of the geometry where the flow remains two-dimensional in the mean sense. The system consists of a double pulsed Nd:Yag laser, an optical system, and a CCD camera (which can record images with 1340×1040 pixels at 10 Hz). The flow is seeded by micron-sized oil droplets provided by a TOPAS spray. Particle images are recorded and processed with a commercial software DAVIS 7.0©. The size of the interrogation area is 32×32 pixels with 50% overlap giving a mesh size of approximately 55 μm. Mean and rms velocity spatial maps are computed by ensemble averaging performed over a set of $N=500$ instantaneous fields. Velocity measurements are conducted at different sections of the channel with $26 < x/e < 46$. The first section $(x/e=26)$ is located near the middle of the channel and the last one $(x/e=46)$ is near the exit.

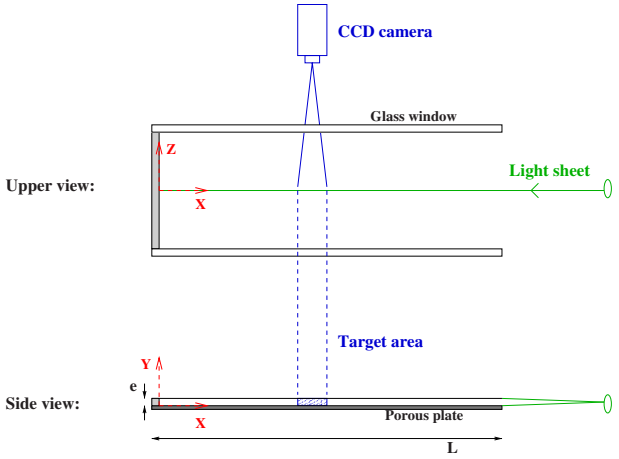

Fig. 3 Principle of PIV measurement

Additional spatial characteristics are obtained by computing a two-point spatial correlation function from instantaneous PIV data. Normalized spatial correlation coefficients are defined by Eq. (1).

$$R_{ii}(\boldsymbol{r}_0,\boldsymbol{r}) = \frac{\overline{u_i(\boldsymbol{r}_0)u_i(\boldsymbol{r}_0+\boldsymbol{r})}}{\sqrt{\overline{u_i^2(\boldsymbol{r}_0)}} \cdot \sqrt{\overline{u_i^2(\boldsymbol{r}_0+\boldsymbol{r})}}} \tag{1}$$

where $\boldsymbol{r}_0$ is a given reference point and i represents the ith component of fluctuating velocity. Two-dimensional spatial maps of R_{ii} for the streamwise and the normal fluctuating velocity are presented in this article.

Supplementary velocity measurements are realized at ambient air with a single hot-wire probe near the exit of the channel $(x/e=46)$. Due to the abundance of books (i.e., Ref. [21]) and articles dedicated to the measure of velocity by hot-wire probe and the classical character of its use for our study, we shall not detail the principle of functioning of this technique. The wire is made of 10% rhodium-platinum, 5 μm in diameter and has a good frequency response up to, at least, 3 kHz.

Mean and turbulent temperature profiles are measured with a cold wire made of platinum (diameter, $d=1$ μm). The probe resistance is about 49 Ω and the current intensity through the wire is near 0.1 mA. In the temperature range of the present experiment, the response of the wire is linear. Temperature measurements are performed at $x/e=46$ near the exit section of the channel.

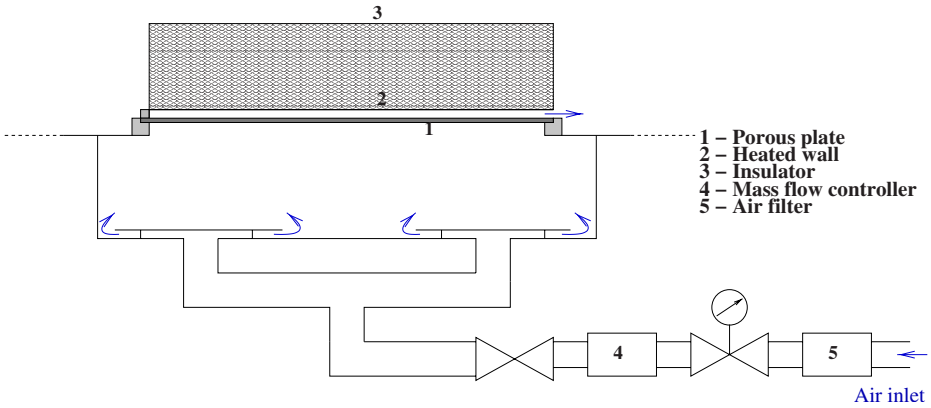

Fig. 2 Experimental setup

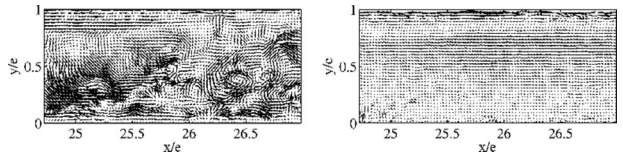

Fig. 4 Instantaneous velocity field at $x/e=26$ for $Re_{in}=189$

3 Dynamic Results

3.1 Turbulence Structure

3.1.1 Instantaneous Fluctuating Velocity Field. Typical instantaneous fluctuating velocity fields measured for both porous plates in the $(x-y)$ plane around $x/e=26$ and at the same Reynolds number are shown in Fig. 4 (the mean velocity field has been removed for clarity). The structure of the fluctuating velocity field is basically different from one plate to another. For the coarse bronze plate, the fluctuating motion exhibits a large downstream coherence length scale, whereas the fluctuating velocity field for the other plate is much more similar to a fully developed classical turbulent channel flow with random eddies of different length scales. This behavior is not completely surprising and is linked to the different porous material microstructures. A microscopic observation of a sintered stainless steel material (Fig. 5) reveals highly random pore configuration, which produces spatial velocity variations (called pseudoturbulence). Previous studies such as Ref. [22] showed that the flow through this type of porous medium seems to coalesce into large scale jets, which affect the flow behavior. The more regular structure of the coarse bronze plate generates less pseudoturbulence but the average pore diameter is bigger and the pore size also influences the levels of spatial velocity variations generated [22,23]. We shall discuss again these characteristics further in this article.

3.2 Mean Velocity—RMS. In order to measure the impact of these microstructural differences in the behavior of the aerodynamic field, we carried out experiments with the two plates by imposing the same total parameters. We present results obtained in section $x/e=26$ for increasing injection Reynolds numbers.

Figure 6 shows the profiles of the mean streamwise velocity normalized by the bulk velocity U_b. The flow features obtained show large differences for the two plates. For the coarse bronze plate, the mean velocity profile is very similar to the laminar one computed by assuming a self-similar profile [11] even if the profile is somewhat disturbed near $y/e=0.3$. According to these predictions, the location of the velocity profile maximum is somewhat shifted toward the upper wall when the Reynolds number is increased. On the other hand, for the fine pore plate, the velocity profile is flatter than for the coarse bronze plate (even for the lowest Reynolds number $Re_{in}=94$); a further increase in the Reynolds number gives a drastic change in the velocity profile, which shows some similarity with a turbulent velocity profile in a classical channel for $Re_{in}=126$, 189, and 220. Larger mean velocity gradients are measured near the porous plate, suggesting an increase in the turbulent activity in this part of the flow. The rms velocity profiles (Fig. 7) are in accordance with previous conclusions. For the coarse bronze plate, the fluctuating velocity profile is nearly uniform (and equally near to the residual rms value due to the dynamic resolution of PIV measurements) except near the upper wall. Nevertheless, it is not clear if the increase in velocity fluctuations near the upper wall for increasing Reynolds numbers are physical or due to unwanted measurement noise. For the fine pore plate, the rms streamwise velocity values can be up to four times higher for a given Reynolds number. The largest fluctuations are measured in the lowest half-part of the channel near the porous plate. Similar trends can be drawn for both plates for the normal velocity fluctuations. The same conclusions are deduced from measurements performed around $x/e=46$: the flow remains nearly laminar for the coarse bronze plate, even if the Reynolds number Re_{in} is increased, while the turbulence is fully developed for the sintered stainless steel plate.

The comparison of the energy spectra in Fig. 8 (obtained with hot-wire probe) calculated for the two types of plates in a given point of the flow and for various injection; Reynolds numbers supplement this description. In accordance with the differences already observed on the mean and RMS velocity profiles, the energy spectra plotted for the fine pore plate are distinguished

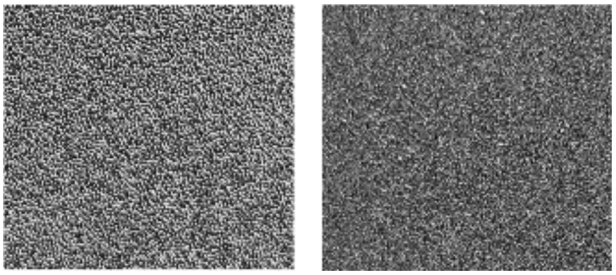

Fig. 5 Porous plates

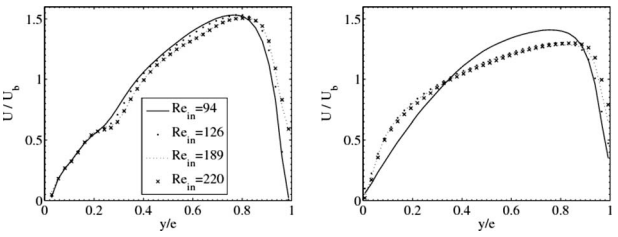

Fig. 6 Mean longitudinal velocity profiles: $x/e=26$

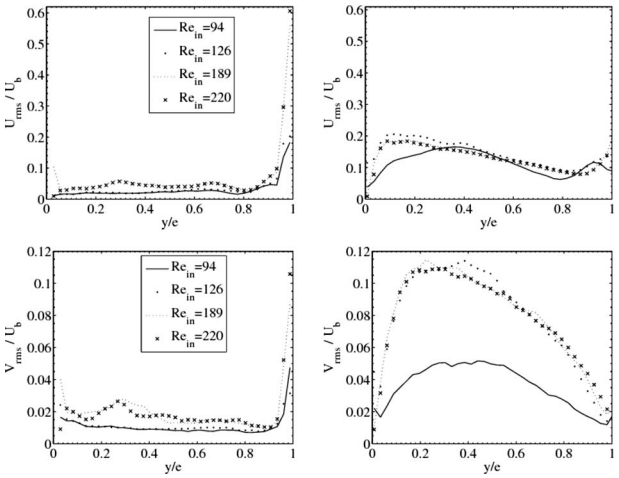

Fig. 7 RMS velocity profiles: $x/e=26$

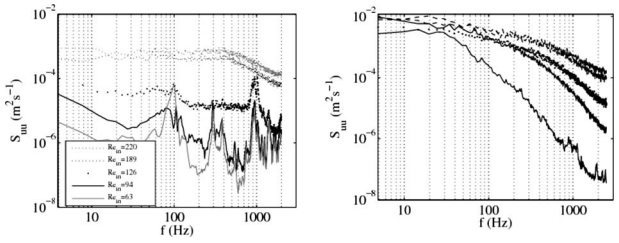

Fig. 8 Energy spectra: $x/e=46$, $y/e=0.65$, and $z/e=0$

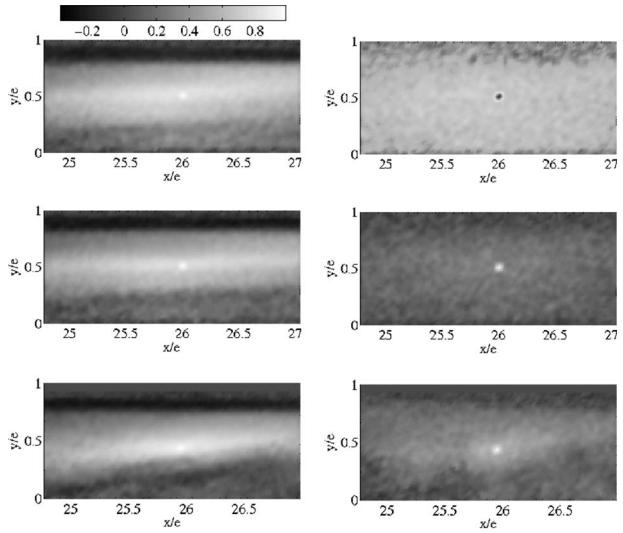

Fig. 9 Coefficients of correlation of the velocity fluctuation for the coarse bronze plate at the point $x/e=26$, $y/e=0.54$, and $z/e=0$

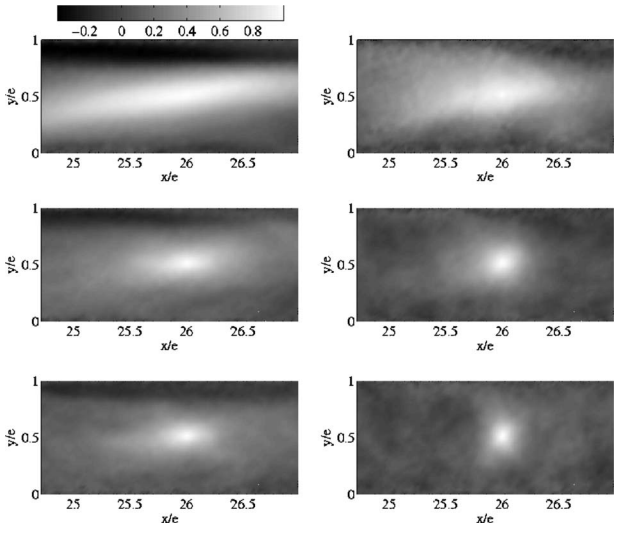

Fig. 10 Coefficients of correlation of the velocity fluctuation for the stainless steel plate at the point $x/e=26$, $y/e=0.54$, and $z/e=0$

clearly from those obtained with the coarse bronze plate: they approach energy spectra corresponding to a developed turbulence. When the Reynolds number increases, the energy enrichment of the spectrum of the fine pore plate is made in a traditional way, i.e., by a progressive increase in the smallest scales whereas for the coarse bronze plate, all the spectra components increase about same manner. The comparison of the energy levels between the two plates for a Reynolds number of $\mathrm{Re}_{in}=63$ shows that the amplitude of the peaks observed with the coarse bronze plate is not of a negligible order of magnitude. In fact, the analysis of the instantaneous velocity fields obtained with the coarse bronze plate shows that the fields are disturbed intermittently; some cartographies represent a regular flow while others let appear disturbed zones. It thus seems that the flow generated by the parietal injection through the coarse bronze plate remains laminar or not very fluctuating at least in the whole of the channel but presents a frequency band spatially amplified visible with small injection Reynolds numbers. This case of figure was encountered by the team of ONERA working on the assembly VECLA (in comparison with Ref. [24]) in the case of a channel of 30 mm height and injection velocities higher than 1 m/s. The comparison between the experimental results and the theory of linear stability are in good agreement, validating the assumption of the development of a hydrodynamic instability in the channel. However, Ref. [25] underlines that some comparisons were less convincing (in particular with a height of channel of 10 mm) and the dissensions observed remain without complete explanation. In our case, the presence of peaks with broad base obtained during our experiment is probably related to the rather important pore diameter of the coarse bronze plate: this characteristic implies a weaker friction loss and therefore a less homogeneous or stable injection in time. Besides, this phenomenon can explain partly the defect noticed in the mean velocity profiles.

3.3 Two Point Spatial Correlation. In the continuity of the previous statistical analyses, we will characterize the coherence of the fluctuating flow by the evaluation of a two-point spatial correlation function defined in the preceding section. Figures 9 and 10 present the results obtained at the point $x/e=26$, $y/e=0.54$, and $z/e=0$ for various injection Reynolds numbers and the two types of plates.

3.3.1 Correlation Function R_{uu}. The isovalues of these coefficients are characterized for the coarse bronze plate (left hand side of Fig. 9) by a strong elongation in the direction of the flow whatever the injection Reynolds number considered: the coefficient is still of the order of 0.5 in the edges of the window of measure. The extension in the direction normal for the wall is also important and decreases with the injection Reynolds number. These maps suggest the existence of large scale orderly movements defined by a strong longitudinal extension. Moreover, this coefficient is asymmetrical according to x property, which characterizes a spatially heterogeneous fluctuation.

For the other plate, the asymmetry of the coefficient R_{uu} (left hand side of Fig. 10) is very pronounced for the weakest Reynolds number: for a distance according to axis x fixed positive, R_{uu} is maximum for an altitude higher at a null altitude. May we remind that this map corresponds to the only case investigated with these plate characterized by a laminar velocity field. The shape of the cartographies changes strongly with the increase in the injection Reynolds number because of a decrease in the longitudinal extension of the correlation.

3.3.2 Correlation Function R_{vv}. For the coarse bronze plate, the fluctuating velocity normal to the wall is perfectly correlated in a quasipunctual zone (right hand side of Fig. 9). However, the levels of correlation still remain important in a big part of the window of measure, for example a wide zone where R_{vv} is of the order of 0.5.

For the other plate, the coefficient is almost circular (right hand side of Fig. 10), characteristics of orderly movements of comparable extension in the directions longitudinal and normal for the wall.

The coefficients of correlation show that the organization of the big structures of the flow is different according to the employed porous plate. Movements with larger scale, sharply superior to the distance between the porous plate and the impermeable plate, are notably observable with the coarse bronze plate. The flow generated by injection through the fine pore plate is characterized by a spatial coherence globally weaker, which decreases with the increase in the injection Reynolds number; this behavior is coherent with the evolution of the spectral densities of energy, which have been previously presented.

We characterize the coherence of the fluctuating flow by the evaluation of a space macroscale of the fluctuating velocity field. We can define scales of spatial length L_{uu} and L_{vv} from the integration on the width $x_{\max}$ of a window of measure of the previous correlations (comparison of Eqs. (2) and (3)).

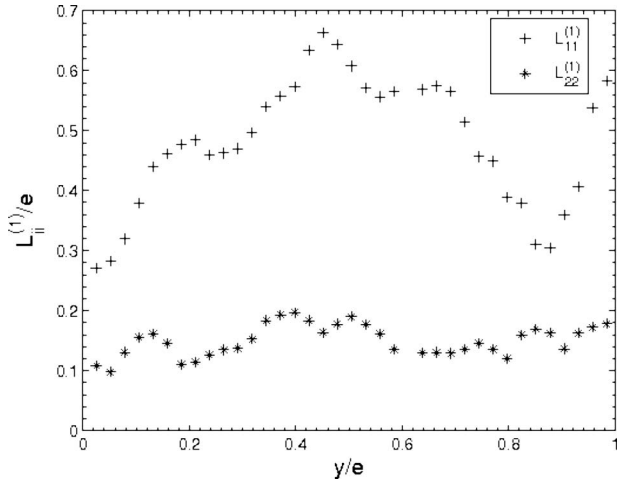

Fig. 11 Spatial length: $Re_{in}=220$ and $x/e=41$

$$L_{uu} = \int_0^{x_{\max}} R_{uu}(x)dx \tag{2}$$

$$L_{vv} = \int_0^{x_{\max}} R_{vv}(x)dx \tag{3}$$

The adimensionnal representation of this spatial length for a measure corresponding to a flow of developed turbulence with the fine pore plate is given by Fig. 11. The scale corresponding to the component normal to the wall is of an order of height lower than the scale associated with the longitudinal component; it is located between $0.1e$ and $0.2e$. The scale L_{uu} grows from the porous wall to reach a maximum of the order of $0.65e$ toward the center of the channel.

In the case of a flat channel, the biggest structures are not located in the center of the channel because of the muddled interaction between these last ones. In our case, it seems that the middle of the channel centralizes a part of the big structures.

3.4 Comparison With RANS Simulation. A comparison with simulations based on a Reynolds stress model is presented. Details about the numerical approach and the model of turbulence used are presented in Refs. [10,20]. In most cases, it is difficult to simulate the geometric details of the porous material surface. Therefore, the porous wall is often replaced by an equivalent material through which the fluid is injected with uniform properties (velocity, temperature, etc.). For the numerical results presented in this paper, the injection is modeled by using additional sources at the porous wall in the resolved equations. A constant source of normal velocity fluctuations characterized by a dimensionless coefficient $\sigma=\sqrt{vv}/V_{in}$, which traduces the level of normal velocity fluctuations at the exit of the porous surface is added. We investigated the influence of $\sigma(0<\sigma<0.5)$ in Refs. [10,20]. We noticed that a more significant turbulence intensity injected at the porous wall shifts the location of the transition due to the basic instability upstream whereas nothing is changed close to the porous wall. These results are consistent with the conclusions of Chaouat and Schiestel [9] who investigated the influence of the pseudoturbulence for a higher injection Reynolds number.

In Figs. 12 and 13, the numerical results obtained with $Re_{in}=94$ and a pseudoturbulence $\sigma=0.2$ are plotted together with the results rising from experiments carried out with the two porous plates. Two sections (in the medium and end of the channel), which are illustrative of all obtained results are presented in this article.

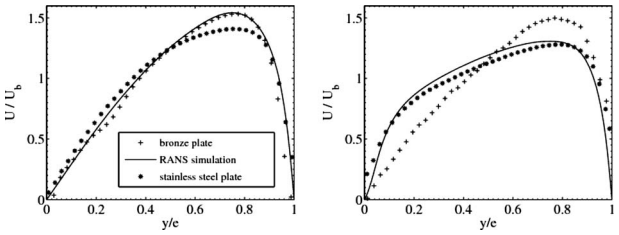

Fig. 12 Mean velocity profiles for $Re_{in}=94$

In the first section $x/e=26$, the mean velocity profiles predicted by simulation are close to those obtained in experiments with the coarse bronze plate. As soon as the profile obtained by numerical simulation changes in form downstream under the effect of an increase in the turbulent fluctuations, this one approaches the experimental curve of the fine pore plate. The observation of the RMS velocity allows to obtain the same conclusions. The general shape and level of the RMS profiles are well reproduced downstream with numerical model.

It thus appears that the two experimental cases cannot be predicted on all the channels studied by numerical simulation based on a RANS model. As the flow obtained with the coarse bronze plate is closer to a transition flow, it is not surprising to note differences between the numerical simulations and the experimental results. The comparison of results seems more justified in the case of the fine pore plate, which provides a more uniform injection. It is known indeed that the microstructure of this plate induces the formation of coalescent jets being able to generate pseudoturbulence. This phenomenon implies a transition to a turbulent state quicker than what they would acquire with a blowing absolutely divided in a uninterrupted manner. Nevertheless, this phenomenon concerns length scale, which remain enough small so that we can model blowing for instance by a uniform source on the condition of including a little of pseudoturbulence. To refine the comparisons between experiment and numerical simulation, it would then be interesting to change the level of pseudoturbulence of the numerical model.

4 Thermal Results

Figure 14 presents mean and RMS temperature profiles at $x/e=46$ for different Reynolds number between 94 and 220. In order to compare the various cases, it is necessary to present results normalized by the temperature difference imposed between the two walls. The evaluation of the injected temperature was carried out by extrapolation of the temperature profiles. As the tempera-

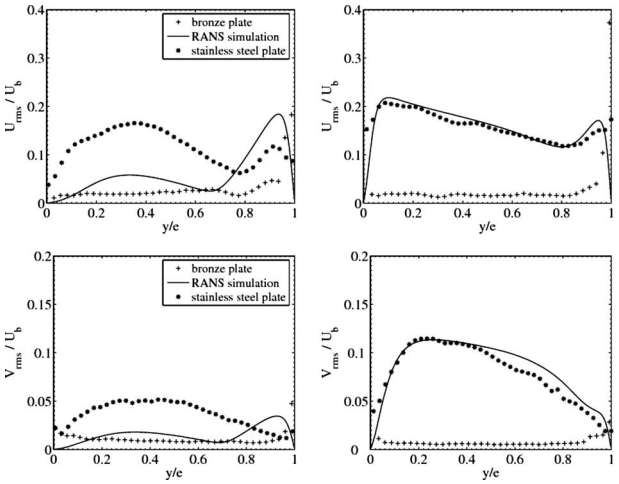

Fig. 13 RMS velocity profiles for $Re_{in}=94$

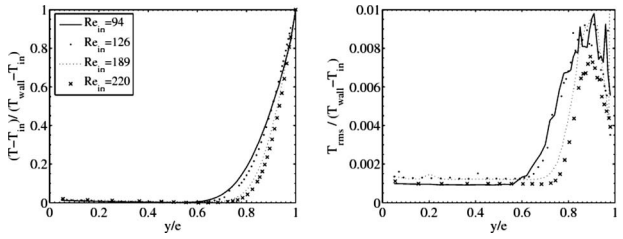

Fig. 14 Left: mean temperature profiles at $x/e=46$; right: RMS temperature profiles at $x/e=46$

ture variation close to the porous wall is almost null, this assessment seems correct. Moreover the confrontation of this value with the result obtained with a thermocouple positioned in the injected box is conclusive. The same method was applied for the temperature of the higher wall. In this case, one probably slightly underestimates the temperature variation and thus the wall temperature.

In all cases, the lower part of the channel (including between $y/e=0$ and $y/e=0.5$) is characterized by a uniform mean temperature, very close to the temperature of the air injected. When the injection Reynolds number increases, this zone extends; in other words, the thickness of thermal boundary layer decreases with the increase in Re_{in}.

We noticed a peak of fluctuations near the higher wall. Apart from this peak, the levels of temperature fluctuations are very low and represent the noise levels of measurement. All the curves present a peak of fluctuations of similar intensity. Only the width of the peak decreases with the increase in the Reynolds number. In order to complete these results, we present on Fig. 15 an assessment of the spectral densities of temperature at $x/e=46$ for two different Re_{in}. Three positions defined by $y/e=0.8$, 0.9, and 0.965, being in the thermal boundary layer, are presented. Spectral densities are normalized by the variance of the temperature fluctuations in order to be able to compare the various series of measurements characterized by different variations in temperature from one wall to the other. The spectral densities traced in the thermal boundary layer are rather similar: we observe a flat zone in the very low frequencies and a cut-off frequency, which decreases with the injection Reynolds number. When the frequency increases, the behavior of the spectral densities shows a fast decrease in the spectral densities on which are superposed amplified frequency bands.

5 Conclusions

The experimental setup of an anisothermal channel flow generated by a porous injection highlights the structural differences in the fluctuating velocity and temperature fields according to the type of porous plate used.

In the range of Reynolds numbers studied, the flow generated by injection through the coarse bronze plate (30% porosity and 100 μm average pore) and the fine pore porous plate (30% porosity and 30 μm average pore diameter) is very different. The flow with the coarse bronze plate is in a large part of the channel slightly fluctuating with a detectable peak of velocity fluctuations and a more important peak of thermal fluctuations close to the upper wall. Movements with large scales were detected. The flow generated by injection through the fine pore plate is on the contrary turbulent. Energy spectra increase in the high frequencies with the Reynolds number, which results in one loss of space coherence.

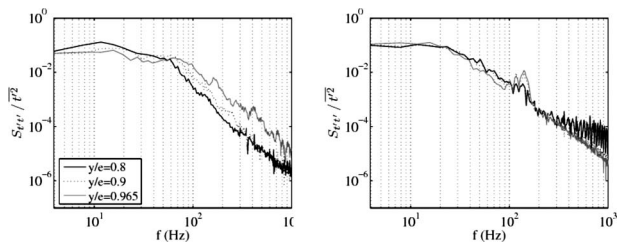

Fig. 15 Spectral densities of temperature

The microstructure of porous material explains partially these differences: the structure of the coarse bronze plate is more regular than the stainless steel material, which generates more pseudoturbulence. The pore diameter is also an essential characteristic of the porous plate and we observed a less homogenous injection in time with the coarse bronze plate.

The comparison of the experimental results with numerical simulations based on a RANS model is consistent with the previous conclusions. The porous wall is modeled by an equivalent material through which the fluid is uniformly injected with a constant source of normal velocity fluctuations. This approach allows to better reproduce the flow generated by the stainless steel plate (more uniform injection and pseudoturbulence) than that generated by the other plate.

In case of engineering applications of protection of surfaces exposed to high temperatures, it is technically difficult to use porous walls with small diameter pores (problem of clogging). Engineers will rather favor the sizes of pores close to those used with the coarse bronze plate.

On the other hand, we conclude that the model of blowing used for the numerical results is very far from the reality for the coarse bronze plate. We could compare our results with LES or DNS like approaches in anisotherm medium to confront our method with problems of hydrodynamics instabilities and transitions of the velocity field.

In order to enhance the description of the temperature fields in the channel, we could perform complementary measures by laser induced fluorescence. This technique will provide the instantaneous temperatures fields in various sections of the channel in a nonintrusive way.

Nomenclature

e = channel height (m)
R = normalized autocorrelation function
Re = Reynolds number
T = temperature (K)
U = streamwise velocity (m s^{-1})
V = normal velocity (m s^{-1})

Subscripts

b = bulk mean quantity
in = condition at injection surface
w = upper wall

References

[1] Taylor, G. I., 1956, "Fluid Flow in Regions Bounded by Porous Surfaces," Proc. R. Soc. London, Ser. A, **234**, pp. 456–475.
[2] Berman, A., 1953, "Laminar Flow in Channels With Porous Wall," J. Appl. Phys., **24**(9), pp. 1232–1235.
[3] Culick, F. E. C., 1966, "Rotational Axisymmetric Mean Flow and Damping of Acoustic Waves in Solid Propellant Rocket Motors," AIAA J., **4**(8), pp. 1462–1464.
[4] Dunlap, R., Willoughby, P. G., and Hermsen, R. W., 1974, "Flowfield in the Combustion of a Solid Propellant Rocket Motor," AIAA J., **12**(10), pp. 1440–1442.
[5] Sabnis, J. S., Madabhushi, H., Gibeling, H. J., and McDonald, H., 1989, "On the Use of $k-\epsilon$ Model for Computation of Solid Rocket Internal Flows," *Proceedings of the 25th Joint Propulsion Conference*, Monterey, CA.
[6] Liou, T. M., Lien, W. Y., and Hwang, P. W., 1998, "Transition Characteristics of Flowfield in a Simulated Solid-Rocket Motor," J. Propul. Power, **14**(3), pp. 282–289.
[7] Avalon, G., Ugurtas, B., Grisch, F., and Bresson, A., 2000, "Numerical Computations and Visualization Tests of the Flow Inside a Cold Gas Simulation With Characterization of a Parietal Vortex Shedding," *Proceedings of the 36th Joint Propulsion Conference and Exhibit*, Huntsville, AL.
[8] Apte, S., and Yang, V., 2001, "Unsteady Flow Evolution in Porous Chamber With Surface Mass Injection, Part 1: Free Oscillation," AIAA J., **39**(8), pp.

1577–1585.
[9] Chaouat, B., and Schiestel, R., 2002, "Reynolds Stress Transport Modelling for Steady and Unsteady Channel Flows With Wall Injection," J. Turbul., **3**(21), pp. 1–15.
[10] Fournier, C., Bataille, F., and Michard, M., 2005, "Transition Characteristics of Flowfield in a Non-Isothermal Duct With Wall Injection," *Proceedings of the Fourth International Conference on Computational Heat and Mass Transfer*, R. Bennacer et al., eds., Tec & Doc, Paris, Vol. 2, pp. 899–904.
[11] Fournier, C., Michard, M., and Bataille, F., 2007, "Heat Transfer in a Laminar Channel Flow Generated by Injection Through Porous Walls," ASME J. Fluids Eng., **129**(8), pp. 1048–1057.
[12] Olson, R. M., and Eckert, E. R. G., 1966, "Experimental Studies of Turbulent Flow in a Porous Circular Tube With Uniform Fluid Injection Through the Tube Wall," ASME J. Appl. Mech., **33**(4), pp. 7–17.
[13] Beddini, R. A., 1986, "Injection-Induced Flows in Porous-Walled Duct," AIAA J., **24**(11), pp. 1766–1773.
[14] Sviridenkov, A. A., and Yagodkin, V. I., 1976, "Flows in the Initial Sections of Channels With Permeable Walls," Fluid Dyn., **13**(5), pp. 43–48.
[15] Chaouat, B., 2002, "Numerical Predictions of Channel Flows With Fluid Injection Using Reynolds-Stress Model," J. Propul. Power, **18**(2), pp. 295–303.
[16] Fournier, C., Michard, M., and Bataille, F., 2003, "Prediction of Heat and Mass Transfer in a Confined Channel Flow With Wall Injection," *Proceedings of the Fourth International Symposium on Turbulence, Heat and Mass Transfer*, Antalya, Turquie, pp. 657–664.
[17] Apte, S., and Yang, V., 2003, "A Large-Eddy Simulation Study of Transition and Flow Instability in a Porous-Walled Chamber With Mass Injection," J. Fluid Mech., **477**, pp. 215–225.
[18] Chaouat, B., and Schiestel, R., 2005, "A New Partially Integrated Transport Model for Subgrid-Scale Stresses and Dissipation Rate for Turbulent Developing Flows," Phys. Fluids, **17**, pp. 1–19.
[19] Deng, Z., and Adrian, R. J., 2002, "Experimental Investigation of a Turbulent Transpiration-Induced Channel Flow Using Particle Image Velocimetry Technique," *Proceedings of the 11th International Symposium on Applications of Laser Techniques to Fluid Mechanics*, Lisbon, Portugal.
[20] Fournier, C., 2005, "Study of Heat and Mass Transfer in a Channel Flow Generated by Blowing Through a Porous Wall," Ph.D. thesis, National Institute of Applied Sciences, France.
[21] Bruun, H. H., 1995, *Hot Wire Anemometer: Principles and Signal Analysis*, Oxford University Press, New York.
[22] Pimenta, M., and Moffat, R. J., 1974, "Stability of Flow Through Porous Plates: Coalescent Jets Effects," AIAA J., **12**(11), pp. 1534–1540.
[23] Ramachandran, N., Heaman, J., and Smith, A., 1992, "An Experimental Study of the Fluid Mechanics Associated With Porous Walls," *Proceedings of the 30th Aerospace Sciences Meeting and Exhibit*, Reno, NV.
[24] Casalis, G., Avalon, G., and Pineau, J. P., 1998, "Spatial Instability of Planar Channel Flow With Fluid Injection Through Porous Walls," Phys. Fluids, **10**(10), pp. 2558–2568.
[25] Griffond, J., 2001, "Instabilité Pariétale et Accrochage Acoustique dans les Conduits Parois Débitantes Simulant les Moteurs á Propergol Solide d'Ariane 5," Ph.D. thesis, Ecole Nationale Supérieure de l'Aéronautique et de l'Espace, Toulouse, France.